PCCP

PAPER

View Article Online
View Journal | View Issue

Cite this: *Phys. Chem. Chem. Phys.*, 2023, **25**, 24081

Unravelling the effect of paramagnetic Ni^{2+} on the ^{13}C NMR shift tensor for carbonate in $Mg_{2-x}Ni_xAl$ layered double hydroxides by quantum-chemical computations†

Megha Mohan,[a] Anders B. A. Andersen,‡[b] Jiří Mareš,[a] Nicholai Daugaard Jensen,[b] Ulla Gro Nielsen *[b] and Juha Vaara *[a]

Structural disorder and low crystallinity render it challenging to characterise the atomic-level structure of layered double hydroxides (LDH). We report a novel multi-step, first-principles computational workflow for the analysis of paramagnetic solid-state NMR of complex inorganic systems such as LDH, which are commonly used as catalysts and energy storage materials. A series of $^{13}CO_3^{2-}$-labelled $Mg_{2-x}Ni_xAl$-LDH, x ranging from 0 (Mg_2Al-LDH) to 2 (Ni_2Al-LDH), features three distinct eigenvalues δ_{11}, δ_{22} and δ_{33} of the experimental ^{13}C chemical shift tensor. The δ_{ii} correlate directly with the concentration of the paramagnetic Ni^{2+} and span a range of $|\delta_{11} - \delta_{33}| \approx 90$ ppm at $x = 0$, increasing to 950 ppm at $x = 2$. In contrast, the isotropic shift, $\delta_{iso}(^{13}C)$, only varies by −14 ppm in the series. Detailed insight is obtained by computing (1) the orbital shielding by periodic density-functional theory involving interlayer water, (2) the long-range pseudocontact contribution of the randomly distributed Ni^{2+} ions in the cation layers (characterised by an *ab initio* susceptibility tensor) by a lattice sum, and (3) the close-range hyperfine terms using a full first-principles shielding machinery. A pseudohydrogen-terminated two-layer cluster model is used to compute (3), particularly the contact terms. Due to negative spin density contribution at the ^{13}C site arising from the close-by Ni^{2+} sites, this step is necessary to reach a semiquantitative agreement with experiment. These findings influence future NMR investigations of the formally closed-shell interlayer species within LDH, such as the anions or water. Furthermore, the workflow is applicable to a variety of complex materials.

Received 29th June 2023,
Accepted 22nd August 2023

DOI: 10.1039/d3cp03053a

rsc.li/pccp

1. Introduction

Layered double hydroxides (LDH) are a class of layered inorganic ionic solids characterised by the general formula $M(II)_{1-x}M(III)_x(OH)_2An_{x/n}{\cdot}yH_2O$, where M(II) [M(III)] is a divalent [trivalent] cation in the metal hydroxide layers, the layers are separated by an interlayer containing anions (An) with a charge of n^- and a variable amount of water.[1–3] The M(III) content, x, ranges between 1/6 and 1/3, hence these materials are often referred to as "M(II)M(III)-LDH". The anions are weakly bound and highly exchangeable, which renders LDH a rare example of anion-exchange materials,[4–7] and therefore allows potential use for, *e.g.*, drug delivery[8] and environmental remediation.[5] Moreover, LDH are used as catalysts[9] and energy materials due to the variable oxidation states of transition metals within the cation layers.[10]

Characterisation of LDH by X-ray diffraction (XRD) is challenging due to structural disorder (such as a mixed M(II) and M(III) occupancy), stacking faults, and interstratification of different polytypes leading to structural ambiguity often combined with nanosized particles.[11] Powder XRD (PXRD), the preferred characterisation technique, only reports on the average structure instead of the detailed local structure. Solid-state NMR (SSNMR) has advanced our understanding of the

[a] *NMR Research Unit, P.O. Box 3000, FI-90014 University of Oulu, Finland. E-mail: juha.vaara@oulu.fi*
[b] *Department of Physics, Chemistry and Pharmacy, University of Southern Denmark, Campusvej 55, DK-5230 Odense, Denmark. E-mail: ugn@sdu.dk*

† Electronic supplementary information (ESI) available: Powder X-ray diffractograms of the $Mg_{2-x}Ni_xAl$-LDH samples, computationally optimised unit cells for the 1M and 2T polytypes, description of the construction of the cluster models for the calculation of the susceptibility of the Ni sites, illustration and coordinates of the clusters, illustration of the calculated spin density in the clusters, coordinates of the sandwich model used to calculate the local hyperfine contribution, experimental and simulated ^{13}C MAS NMR spectra, NMR parameters reported in the Haeberlen convention, the calculated orbital shielding tensors, local hyperfine shielding tensors obtained from a sandwich cluster model, as well as figures and tables of computational ^{13}C shielding tensor eigenvalues by methods 2 and 3 described in the text. See DOI: https://doi.org/10.1039/d3cp03053a

‡ Present address: Department for Nuclear Medicine, Herlev Hospital, Borgmester Ib Juuls Vej 71, DK-2730 Herlev, Denmark.

atomic-level structure of LDH, especially the local structure of the cation layer and the disordered and dynamic interlayer.[12] For example, ^{1}H magic-angle spinning (MAS) NMR using ultrafast rotation has confirmed cation ordering in the metal hydroxide layer (Al–O–Al avoidance)[13] and the metal-ion distribution in trimetallic $Mg_{2-x}Ni_xAl$-LDH.[14] SSNMR has also given insight into the highly disordered interlayer, such as revealing a dynamic exchange between carbonate and bicarbonate,[15] as well as CO_2 exchange with the atmosphere.[16]

The most detailed crystal structures have been obtained from single-crystal XRD studies of MgAl-LDH minerals with carbonate (CO_3^{2-}) as anion. These have, for quintinite ($Mg_4Al_2(OH)_{12}CO_3{\cdot}3H_2O$) – a MgAl-LDH with a Mg : Al ratio of 2 : 1, confirmed ordering of the metal ions.[17] The crystal structure of such a LDH is illustrated in Fig. 1, involving a "honeycomb" cation layer structure for both known quintinite polymorphs (1M and 2T).[17,18] The 1M and 2T polymorphs differ in the stacking of the cation layers. The interlayer has a high degree of structural disorder, which is reflected by the presence of multiple carbonate sites and water sites with partial occupancy for both structures. Recently, a combination of Rietveld refinement of PXRD data and multi-nuclear SSNMR also confirmed a lowering of the space group symmetry to monoclinic for ZnAl-LDH with carbonate in the interlayer.[19] Furthermore, both carbonate and bicarbonate (HCO_3^-) have been identified in the interlayer of diamagnetic MgAl-LDH, where the high Al content (high cation layer charge) favours carbonate.[15] These two anions can be distinguished based on a 10 ppm difference in the ^{13}C isotropic chemical shift, $\delta_{iso}(^{13}C)$, opposite signs of the ^{13}C chemical shift anisotropy and assignment based on a visual comparison with the ^{13}C MAS NMR spectra of sodium carbonate and bicarbonate in MgAl-LDH[15] and calcinated MgAl-LDH.[20]

While SSNMR has successfully probed the local structure of diamagnetic LDH,[12] the presence of paramagnetic species renders the analysis of SSNMR spectra more challenging. Significant paramagnetic shifts are observed for ^{27}Al in LDH, $\delta_{iso}(^{27}Al)$, with Co^{2+}, Ni^{2+} and Cu^{2+}.[14,21] While the $\delta_{iso}(^{27}Al)$ in a series of $Mg_{2-x}Ni_xAl(OH)_6(CO_3){\cdot}nH_2O$, with x ranging from 0 to 2, was shown to scale linearly with the number of Ni^{2+} ions that neighbour Al in the metal layer (*ca.* −350 ppm/Ni), the total Ni content (Ni:Al ratio) and interlayer spacing only had a small effect in NiAl-LDH.[14] Furthermore, only small paramagnetic shifts (<20 ppm) have been observed for carbonate in NiAl-LDH[22] and phosphate MgFe-LDH.[23] In these studies, only the isotropic shifts determined from visual inspection of the NMR spectra were reported and no detailed analyses of the NMR spectra have so far been performed. Such analyses can benefit immensely from computational and theoretical methods in the assignment and interpretations of paramagnetic NMR spectra.

Understanding the structure of LDH, including the atomic detail and the effect of paramagnetic doping, is central to link the atomic level structure and materials properties, a pivotal challenge in materials science. This information can now be extracted for diamagnetic systems using SSNMR and first-principles modelling ("NMR crystallography").[24] In contrast,

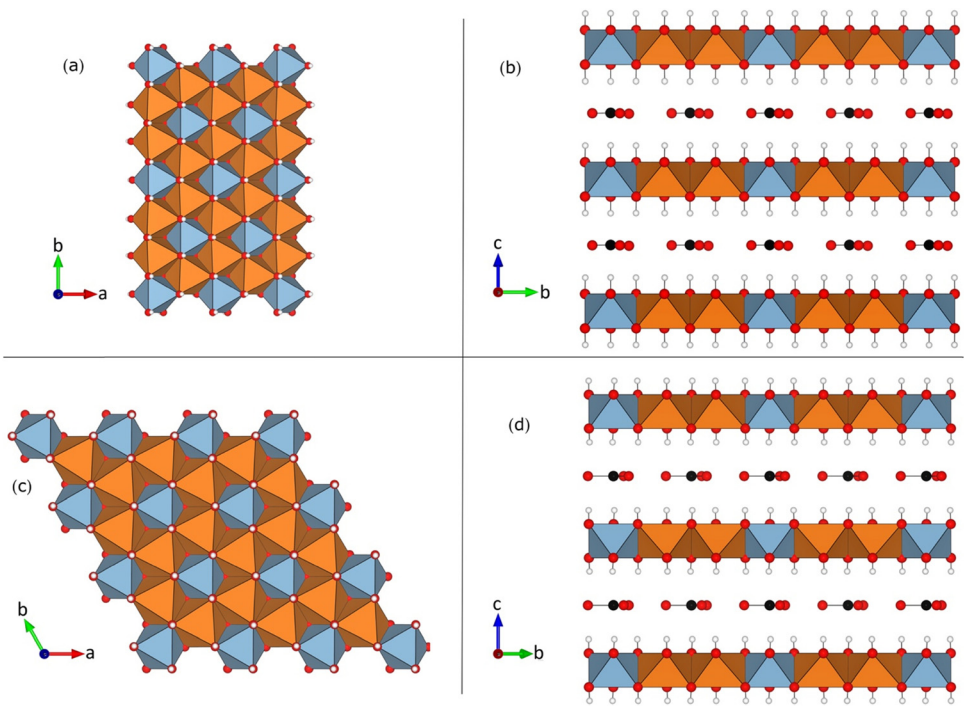

Fig. 1 Crystal structure of the Mg_2Al-LDH studied in this paper: (a) and (b) 1M and (c) and (d) 2T polytypes illustrating the "honeycomb" superstructure, where all Al (blue) are surrounded by Mg (orange).[17,18] View along the LDH layer normal direction in panels (ac) and along one of the in-layer axes in (b) and (d). Representative examples of the interlayer CO_3^{2-} anions are shown, and the interlayer water molecules have been omitted. In the cation layers, the blue (orange) polyhedra correspond to Al (Mg) sites.

analysis of SSNMR spectra of paramagnetic systems, commonly found in battery, catalytic, and magnetic materials, are challenging. Here we focus on how the concentration of paramagnetic Ni^{2+} ions in LDH affects the ^{13}C SSNMR spectra of the interlayer carbonate anions. To develop the methodology, we have performed ^{13}C SSNMR measurements of the samples in the solid solutions $Mg_{2-x}Ni_xAl(OH)_6(CO_3)_{0.5}{\cdot}nH_2O$, a series of hydrotalcite-type LDH with x = 0, 0.18, 0.34, 0.68, 0.86 and 2. In this series, a specific percentage of diamagnetic Mg^{2+} ions are replaced by paramagnetic Ni^{2+} ions carrying two unpaired electrons (S = 1). Such Ni-doped MgAl-LDH are used as precursors for industrial catalysts. A ^{27}Al MAS NMR study of the closely related $Mg_{2-x}Ni_xAl(OH)_6(NO_3){\cdot}nH_2O$ series showed cation ordering implying Al–O–Al avoidance, and a random (binomial) distribution of Ni^{2+} and Mg^{2+} on the M(II) site.[14] The latter reflects the similar ionic radii of Ni^{2+} (55 pm) and Mg^{2+} (57 pm). Detailed analyses of the ^{13}C MAS NMR spectra reveals one principal ^{13}C site (see, however, below) with both anisotropy and rhombicity (asymmetry) of the ^{13}C shielding tensor, with the anisotropy scaling linearly with the Ni^{2+} concentration. In contrast, the isotropic chemical shift, $\delta_{iso}(^{27}Al)$, only slightly decreases with Ni doping. A recent solid-state ^{13}C MAS NMR study of a $Mg_{1-x}Ni_x$ metal–organic framework material[25] found signatures of eight local environments with distinct arrangement of Ni^{2+} ions in the close vicinity of the ^{13}C centre, and revealed a non-random distribution of nickel metal sites resulting from ferromagnetic and antiferromagnetic couplings between the Ni^{2+} ions. As noted above, the present $Mg_{2-x}Ni_xAl$-LDH materials bear no such indications of magnetic couplings. To understand the paramagnetic ^{13}C shifts in the present systems, we compute the pseudocontact shift tensor over a large number of realisations of the random Ni^{2+} distribution for each of the studied Ni concentrations, by a point-dipole approximation (PDA).[26] However, it is found that qualitative agreement with the experimental shielding tensor is only obtained if the local hyperfine contributions resulting from the spin density distribution of the nearby Ni^{2+} sites, which extends to the interlayer anions, are included in addition to the (expected) local orbital and non-local pseudocontact contributions.

2. Experimental data

Samples

The $Mg_{2-x}Ni_xAl$-LDH samples (x = 0, 0.18, 0.34, 0.68, 0.83 and 2) were prepared by ion exchange with ^{13}C-labelled carbonate using the corresponding $Mg_{2-x}Ni_xAl$-LDH with nitrate (NO_3^-) in the interlayer. The preparation of the parent $Mg_{2-x}Ni_xAl$-LDH samples has been reported earlier. The parent Mg_2Al-LDH with chloride as the interlayer ion was prepared by co-precipitation at constant pH.[27] Typically, *ca.* 200 mg of the LDH was suspended in a solution of *ca.* 0.40 g sodium bicarbonate in 20 mL of deionised water for 24–48 h, followed by separation by filtering and drying at 60 °C overnight. PXRD confirmed the intercalation of carbonate and preservation of the LDH (see Fig. S1 in the ESI†). While the PXRD diffractograms of polycrystalline (powder) LDH samples show the characteristic features for stacking disorder, *i.e.*, interstratification of different polymorphs, the complexity prevents further analysis. ^{13}C-enriched (99%) sodium carbonate (Na_2CO_3) and sodium bicarbonate ($NaHCO_3$) were obtained from Sigma-Aldrich and used as received.

Solid-state ^{13}C MAS NMR experiments

Solid-state ^{13}C MAS NMR experiments were performed on an Agilent 600 MHz NMR spectrometer (14.1 T) using a 3.2 mm HXY MAS NMR probe tuned to ^1H and ^{13}C in double-resonance mode. Adamantane was used as a secondary chemical shift reference, with $\delta(CH)$ = 38.3 ppm with respect to TMS (0 ppm). ^{13}C MAS NMR spectra of the paramagnetic (Ni-containing) samples were acquired using a Hahn-Echo sequence (90°-τ-180°-τ-acquisition, τ = 1 rotor period) without ^1H decoupling, 10 kHz spinning speed, and with a 90° (180°) pulse of 2.2 (4.4) μs, a relaxation delay of 1 s and 5000–40 000 scans. The relaxation time was measured for $Mg_{2-x}Ni_xAl$-LDH with x = 0.16 to determine the maximum relaxation time needed to ensure quantitative spectra. $^{13}C\{^1H\}$ CP-MAS spectra were recorded for the diamagnetic Mg_2Al-CO_3 (7 s relaxation delay, 7000 scans) and $NaHCO_3$ (2 s relaxation delay, 8 scans) using a ramped CP sequence with spinning speeds in the range 3–10 kHz and 5 ms contact time, whereas a single-pulse ^{13}C MAS NMR spectrum was recorded for Na_2CO_3 (30° pulse, 8 scans, and 900 s relaxation delay). We note that a Hahn-echo sequence or CP was necessary to suppress a large ^{13}C background signal from Kel-F, a fluorinated polymer, in the MAS NMR probe. The magic angle was carefully set by minimising the linewidth of the spinning sidebands from ^{79}Br in KBr. The spectra were processed and analysed using ssNake.[28]

3. Computational methods

In previous experiments,[14] the ^{27}Al NMR chemical shift within the cationic layer of in $Mg_{2-x}Ni_xAl$-LDH scales linearly with the number of neighbouring, paramagnetic Ni^{2+} ions. This implies insignificantly small exchange coupling[29] between such sites at the measurement temperature, hence the paramagnetic NMR effects caused by the Ni^{2+} ions on the interlayer anions can be considered additive. The model followed in the present computations of the ^{13}C NMR shielding tensors of the interlayer carbonate anions makes use of this; a flow diagram of the computational procedure is given in Fig. 2.

In a paramagnetic substance, the NMR shielding tensor is traditionally decomposed as[26]

$$\boldsymbol{\sigma} = \boldsymbol{\sigma}_{orb} + \boldsymbol{\sigma}_{con} + \boldsymbol{\sigma}_{pc}, \quad (1)$$

where $\boldsymbol{\sigma}_{orb}$ is the orbital shielding tensor that mainly results from the immediate chemical environment of the NMR nucleus, $\boldsymbol{\sigma}_{con}$ consists of the hyperfine contributions within the reach of the unpaired electron spin density distribution (with the contact term playing a big role), and $\boldsymbol{\sigma}_{pc}$ is the "through-space" pseudocontact contribution outside that area.

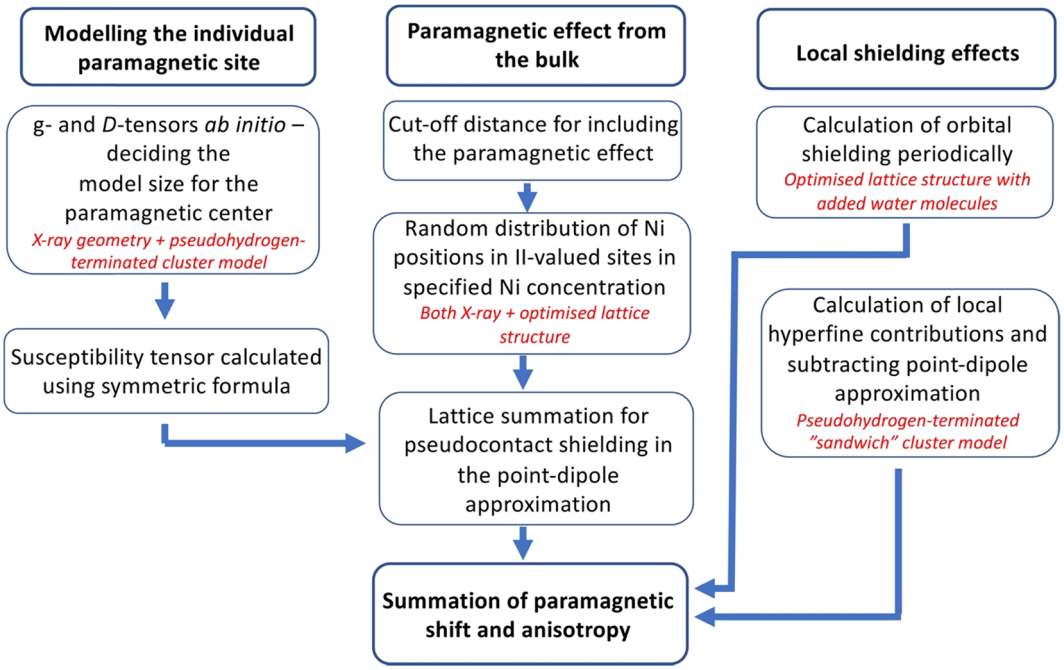

Fig. 2 Flow diagram of the chemical shift modelling performed in this work.

All these contributions are evaluated presently for ^{13}C in the carbonate anion.

As the NMR spectra of the materials are strongly affected by the paramagnetic Ni^{2+} dopants randomly introduced on the M(II) sites, we average the pseudocontact shielding $\boldsymbol{\sigma}_{pc}$ over a large number of different random Ni^{2+} distributions at each Ni concentration. For this, we create a PDA model of an individual Ni^{2+} site by assigning it a magnetic susceptibility tensor calculated *ab initio* using correlated wave function theory. We carry out lattice summations of $\boldsymbol{\sigma}_{pc}$ over the Ni^{2+} distributions using experimental X-ray structures for both 1M and 2T structures (see below), as well as (for comparison) corresponding, computationally optimised structures obtained using a density-functional theory (DFT)/plane-wave pseudopotential method for the diamagnetic Mg_2Al-LDH end member of the present LDH series. Finally, a cluster model of the immediate surroundings of the interlayer carbonate is created, in which the anion is sandwiched between the "above" and "below" cationic layers, for calculating the close-range $\boldsymbol{\sigma}_{con}$ contributions.

Crystal structures

Two high-quality single-crystal X-ray structures of quintinite, $Mg_4Al_2(OH)_{12}(CO_3)(H_2O)_3$, from the work of Zhitova *et al.* have been selected: the 1M structure[17] and the 2T structure[18] representing the two different polytypes, which differ in their layer stacking. Visualization of the 1M and 2T crystal structures were produced with VESTA (ver. 3.5.8).[30] In 1M,[17,31] the cation layers are ordered with a rhombohedral stacking sequence, whereas in 2T a hexagonal stacking sequence is found. Both structures contain a highly ordered cation layer with an ideal honeycomb structure where each Al is surrounded by 6 Mg sites (implying Al–O–Al avoidance), as evidenced by the observation of superlattice reflections by XRD. In contrast, the interlayer carbonate anions and water are highly disordered. The 1M structure crystallises in the space group $C2/m$ and the 2T with $P\bar{3}c1$, both with a single Al and Mg crystallographic site. The interlayer of the 1M structure contains two crystallographic inequivalent carbon centres (carbonates),[18] whereas the 2T structure has 3 crystallographic inequivalent carbons. A large variation is shown in the local hydrogen-bonding environment for carbonate even within the same structure. For example, the two carbon sites of the 1M structure have C_{2v} symmetry and 1 water molecule, all with approximately 1/12 occupancy within the experimental error of the refinement. Similarly, the 2T structure[17] features three highly disordered carbonate anions and one water molecule in the interlayer, with occupancy ranging from 0.08 (2T/C2) to 0.14 (C1, C3).

To gain a practical computational model for geometry optimisations and calculating $\boldsymbol{\sigma}_{orb}$, unit cells were built for the CASTEP code[32] from the cif-file obtained from the published single crystal X-ray structures into which explicit carbonate and water molecules were put in place, instead of the partially occupied carbonates and waters to match the chemical formula of $Mg_4Al_2(OH)_{12}(CO_3)\cdot 3H_2O$. Thus, three water molecules per carbonate were inserted. Whereas the 1M cell contain two crystallographic inequivalent carbon sites as in the original cif file, the practical realisation of the 2T cell contains four crystallographic inequivalent carbons, *i.e.*, one of the original inequivalent carbon sites of the X-ray structure is in the computations represented by two carbons (the 2T/C1 and 2T/C3 sites). The resulting 1M and 2T unit cells (both atomic positions and unit cell parameters) were then geometry-optimised in CASTEP without symmetry restrictions using the PBE functional[33] empirical dispersion correction of the Grimme

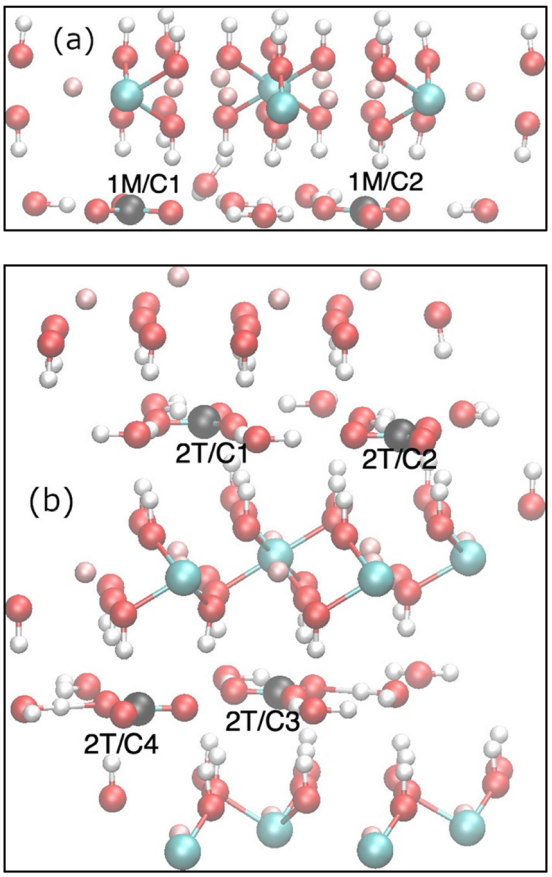

Fig. 3 Computationally optimised unit cells of the (a) 1M and (b) 2T simulation cells with the individual ^{13}C sites indicated.

G06 type,[34] Koelling–Harmon treatment of scalar relativistic effects,[35] and the large plane-wave cut-off of 630 eV. The supercell contained 86/172 ions for the 1M/2T structures, and the *k*-space was sampled by a Monkhorst–Pack grid[36] with 0.1 Å^{-1} spacing. The optimised geometries for the 1M and 2T structures are given in the ESI,† Tables S1 and S2. In the geometry optimisations, the Mg_2Al-LDH end member (x = 0) was used. Fig. 3 illustrates the optimised structures for 1M and 2T, with the different ^{13}C sites indicated.

Orbital shielding

CASTEP[37,38] was subsequently used to calculate the orbital shielding tensors $\boldsymbol{\sigma}_{\mathrm{orb}}$ of the two (1M/C1-2) or four (2T/C1-4) carbon sites in the optimised, diamagnetic Mg_2Al-LDH geometry, with water molecules present. Similar computational choices were made as for the geometry optimisation. The numerical precision was checked by carrying out the entire process (including geometry optimisation and the shielding tensor computation) twice, using the increased cut-off of 900 eV and denser *k*-point sampling (with 0.08 and 0.05 Å^{-1} spacing of the Monkhorst–Pack grid for 1M and 2T, respectively) on the second time. The two series of calculations showed maximum changes of the order of 1 ppm in the resulting components of $\boldsymbol{\sigma}_{\mathrm{orb}}$, and the better of these two sets of calculations (which we use in the following) can be considered well-converged. As the water molecules were manually added to the positions in between the carbonate ions, an element of non-generality remains in their arrangement and, thus, the hydrogen-bonding situation of the carbonate ions. The resulting local environments are described below. The calculated eigenvalues of orbital shielding tensor $\boldsymbol{\sigma}_{\mathrm{orb}}$ were converted to the chemical shift eigenvalues δ_{ii} (i = 1–3) by subtracting from the isotropic ^{13}C shielding constant of TMS, σ_{C} = 179 ppm, obtained using similar methodology in CASTEP.

Pseudocontact shielding

Pseudocontact shielding was calculated using a PDA model that assumes that the NMR nucleus is far enough from the centre with unpaired electrons, so that the contact-type and other interactions that depend on the extent of delocalisation of the electron spin no longer influence the shielding (this turned out to be insufficient, *vide infra*). The paramagnetic metal site is in this model furnished with a susceptibility tensor that can be calculated from the *g*-tensor and the zero-field splitting (ZFS) tensor of that centre[26] as:

$$\boldsymbol{\chi} = \frac{\mu_0 \mu_{\mathrm{B}}^2}{kT} \boldsymbol{g} \cdot \langle \boldsymbol{SS} \rangle \cdot \boldsymbol{g}^T \qquad (2)$$

Here, $\boldsymbol{g}$ is the *g*-tensor, $\langle \boldsymbol{SS} \rangle$ is the dyadic of the effective spin operator $\boldsymbol{S}$,[39] and the other symbols have their usual meanings. The pseudocontact shielding at the site of the distant NMR nucleus is calculated from the susceptibility and the relative position of the NMR nucleus with respect to the paramagnetic centre as

$$\boldsymbol{\sigma}_{\mathrm{pc}} = -\frac{1}{4\pi r^3} \boldsymbol{\chi} \cdot \left(3\frac{\boldsymbol{rr}}{r^2} - \mathbf{1} \right), \qquad (3)$$

where $\boldsymbol{r}$ is the vector (with length r) from the paramagnetic centre to the NMR nucleus. PDA can be seen, for nuclei that reside far from the spin-density distribution, as an alternative to the full quantum-chemical calculation of the pNMR shielding tensor (see below).[39–42] While PDA has been routinely used in analysis of NMR data,[26] only recently it was shown[43] in a detailed way how the susceptibility formalism follows from the full quantum formalism. In particular, the symmetric form of the susceptibility, with the *g*-tensor occurring twice (and not once[44]) in eqn (2) above, is obtained by considering the long-distance limiting forms of both the spin-dipole and orbital hyperfine operators.

Susceptibility of the Ni^{2+} site

We constructed finite molecular cluster models cut out from the LDH layers for computing $\boldsymbol{\chi}$ for an isolated paramagnetic Ni site. Three different-size cluster models (''small'', ''medium'' and ''large''), each centred at the Ni^{2+} ion and extending to an increasing number of neighbouring metal sites, were constructed and subjected to pseudohydrogen termination.[45] The process was performed similarly as in a recent paper[46] and the present details as well as the resulting clusters can be found in the ESI.† The Ni sites have cylindrical symmetry, hence the unique axes of the *g*-tensor, the ZFS tensor and the resulting $\boldsymbol{\chi}$

all coincide with the layer normal direction. With such a cylindrically symmetric susceptibility, the contribution from a single paramagnetic Ni^{2+} centre to the shielding tensor of a distant NMR nucleus in the PDA becomes

$$\boldsymbol{\sigma}_{\mathrm{pc}} = -\frac{3}{4\pi r^3}\begin{pmatrix} \left(\chi-\frac{\Delta\chi}{3}\right)\left(\sin^2\theta\cos^2\phi-\frac{1}{3}\right) & \left(\chi-\frac{\Delta\chi}{3}\right)\sin^2\theta\sin\phi\cos\phi & \left(\chi-\frac{\Delta\chi}{3}\right)\sin\theta\cos\theta\cos\phi \\ \left(\chi-\frac{\Delta\chi}{3}\right)\sin^2\theta\sin\phi\cos\phi & \left(\chi-\frac{\Delta\chi}{3}\right)\left(\sin^2\theta\sin^2\phi-\frac{1}{3}\right) & \left(\chi-\frac{\Delta\chi}{3}\right)\sin\theta\cos\theta\sin\phi \\ \left(\chi+\frac{2\Delta\chi}{3}\right)\sin\theta\cos\theta\cos\phi & \left(\chi+\frac{2\Delta\chi}{3}\right)\sin\theta\cos\theta\sin\phi & \left(\chi+\frac{2\Delta\chi}{3}\right)\left(\cos^2\theta-\frac{1}{3}\right) \end{pmatrix}, \quad (4)$$

where χ and $\Delta\chi = \chi_{\parallel} - \chi_{\perp}$ are the isotropic susceptibility and susceptibility anisotropy with respect to the direction normal to the LDH layers, and the spherical polar coordinates r, θ, and ϕ define the relative position of the NMR nucleus with respect to the paramagnetic site.

The g- and ZFS tensors were calculated for the optimised structures of the single Ni^{2+}-site models using the ORCA software[47] at the state-average complete active space (SA-CASSCF) level using eight electrons in the five orbitals [CAS(8,5)] arising from the 3d shell of the metal ion. The calculations included 10 and 15 states in the triplet and singlet manifolds, respectively. The one-component wave functions were optimised using the scalar relativistic second-order Douglas–Kroll–Hess (DKH2) Hamiltonian[48,49] after which the spin–orbit Hamiltonian was diagonalised in the basis of the SA-CASSCF wave functions in a quasi-degenerate perturbation theory process, to calculate the magnetic properties.[50,51] In addition, the strongly contracted N-electron valence-state perturbation theory of second order (NEVPT2)[52–54] could be applied to the smallest of the three models for the Ni centre, to estimate dynamical correlation effects. The results in Table 1 indicate that the (expected cylindrically symmetric) g- and ZFS tensors, as well as the resulting susceptibility, converge rapidly with the model size. This reflects the localised electron spin density distribution, which houses the spin-density distribution well within its confines (Fig. S3, ESI†). The isotropic g-value at the CASSCF (NEVPT2) level is obtained as 2.27 (2.21), and the corresponding result for the g-tensor anisotropy $g_{\parallel} - g_{\perp}$ is 0.04 (0.03). The D-parameter of the ZFS equals −6.6 (−4.7) cm^{-1}, indicating a moderately easy-axis magnetic nature of the Ni centre. Similar first-principles methodology was recently used for the individual Ni^{2+} sites in nickelalumite ($NiAl_4(OH)_{12}SO_4 \cdot 3H_2O$), an LDH mineral, resulting in very similar data: g = 2.24, g-anisotropy 0.05 and D = −7.8 cm^{-1}, for which very good agreement was observed with experimental values.[46] Due to the good convergence with the model size, in the present paper we used $\boldsymbol{\chi}$ resulting from the NEVPT2 calculations of the small model, for the calculations of $\boldsymbol{\sigma}_{\mathrm{pc}}$.

Lattice summation

$\boldsymbol{\sigma}_{\mathrm{pc}}$ was obtained as a lattice sum of eqn (4) over all paramagnetic Ni^{2+} sites that resided within a 70 Å cut-off distance from the ^{13}C sites. The cut-off was selected in test calculations in which we found the total $\boldsymbol{\sigma}_{\mathrm{pc}}$ to be converged to *ca.* 1% with the present choice. As the distribution of the Ni doping in the LDH layers is random, one cannot expect to reproduce the experimental data using any a single structure of the paramagnetic defects. Consequently, we averaged $\boldsymbol{\sigma}_{\mathrm{pc}}$ over 3000 randomly chosen distributions of the Ni ions onto the M(II) sites. While the $\boldsymbol{\sigma}_{\mathrm{orb}}$ were always obtained for the computationally optimised 1M or 2T models including the interlayer water molecules, the lattice sums of $\boldsymbol{\sigma}_{\mathrm{pc}}$ were carried out using the M^{2+} positions from both the original X-ray structures and the computationally optimised CASTEP structures. A temperature of 300 K was used in all the computations.

Close-range shielding model

To calculate the $\boldsymbol{\sigma}_{\mathrm{con}}$ term of eqn (1), we constructed a local cluster model of the immediate surroundings of CO_3^{2-} including, in addition to the ion itself, "small" (in the same nomenclature as used above for in the calculation of $\boldsymbol{\chi}$) clusters of both adjacent cationic layers. The model is depicted in Fig. 4 and the atomic coordinates are given in Table S7 in the ESI.† The atomic positions were adopted from the periodically optimised 1M unit

Table 1 The computed eigenvalues of the g-tensor, the D- and E-parameters of zero-field splitting, as well as the resulting isotropic average χ and the off- and in-plane components, $\chi_{\parallel}$ and $\chi_{\perp}$, respectively, of the susceptibility tensor at the CASSCF level in local models of different sizes of paramagnetic Ni^{2+} impurity centres (see Fig. S2 in the ESI) in the layers of Mg_2Al-LDH

	g-Tensor			ZFS		Susceptibility (10^{-32} m^3)		
Model	$g_{\parallel}$	$g_{\perp}$	g	D/cm^{-1}	E/D	$\chi_{\parallel}$[a]	$\chi_{\perp}$[a]	χ
Small[b]	2.301 (2.229)	2.258 (2.197)	2.272 (2.208)	−6.561 (−4.740)	0.0000 (0.0001)	9.303 (8.709)	8.823 (8.368)	8.983 (8.482)
Medium	2.301	2.259	2.273	−6.429	0.0000	9.301	8.831	8.988
Large	2.300	2.260	2.273	−6.286	0.0000	9.297	8.837	8.990

[a] The susceptibility anisotropy appearing in eqn (4) is obtained as $\Delta\chi = \chi_{\parallel} - \chi_{\perp}$. [b] Results at the NEVPT2 level in parentheses.

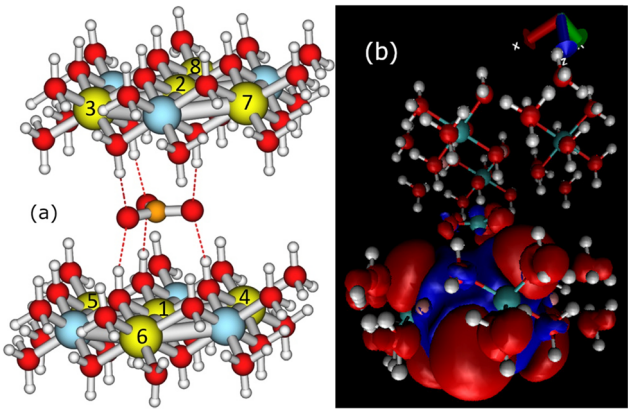

Fig. 4 (a) The cluster model used in the calculation of the close-range hyperfine contributions to the paramagnetic ^{13}C shielding tensor of the interlayer carbonate. The numbering of the paramagnetic sites corresponds to Table 4. (b) The spin density distribution obtained with the paramagnetic Ni located closest to the carbon centre, *i.e.*, position 1 in Table 4. Positive (negative) isosurfaces are shown in red (blue) with the isovalue of 10^{-5} a.u.

cell from which the clusters representing the cationic layers were cut out and terminated by pseudohydrogens, as discussed above. Since the local structure of the 1M and 2T polymorphs are similar and mainly differ in the stacking of the cation layers, we used the same local model for both 1M and 2T lattices.

There are eight M(II) sites in the local model, four on each side of the interlayer carbonate, and we occupied each of these eight sites in turn by the paramagnetic Ni^{2+} centre with the other seven occupied with diamagnetic Mg^{2+}. From each of the single-centre paramagnetic models we calculated the full hyperfine part $\boldsymbol{\sigma}_{hf}$ of the paramagnetic shielding tensor using Kurland–McGarvey theory[40] as

$$\boldsymbol{\sigma}_{hf} = -\frac{\mu_B}{\gamma k T}\boldsymbol{g}\cdot\langle \boldsymbol{SS}\rangle\cdot\boldsymbol{A}, \quad (5)$$

where γ and $\boldsymbol{A}$ are the gyromagnetic ratio and hyperfine coupling tensor of the ^{13}C centre. The g- and ZFS tensors of the small cluster model of the cationic layer, obtained at the NEVPT2 level as described above, were used. $\boldsymbol{A}$ was obtained at the scalar relativistic DKH2 level using DFT/PBE0 level with the DKH-def2-TZVP basis[55] for the cluster atoms and DKH-def2-SV(P) for the terminating pseudohydrogens, on the ORCA code including the contact, dipolar and orbital hyperfine contributions. As the paramagnetic centre in all these eight calculations was already included in the above-described lattice summations of $\boldsymbol{\sigma}_{pc}$, we subtracted from $\boldsymbol{\sigma}_{hf}$ the corresponding PDA contribution $\boldsymbol{\sigma}_{pc}{}^{(1)}$ from the same centre, to avoid double counting: $\boldsymbol{\sigma}_{con} = \boldsymbol{\sigma}_{hf} - \boldsymbol{\sigma}_{pc}^{(1)}$. Finally, the contributions from the eight paramagnetic centres of the local model were summed up, to get the total close-range hyperfine shielding contribution corresponding to the case of 100% Ni^{2+} substitution (x = 2). As we assume that the occupation of the Ni^{2+} sites is completely random, we obtain the close-range contribution to the different levels of Ni-ion doping by multiplying the result by the fractional Ni^{2+} occupation.

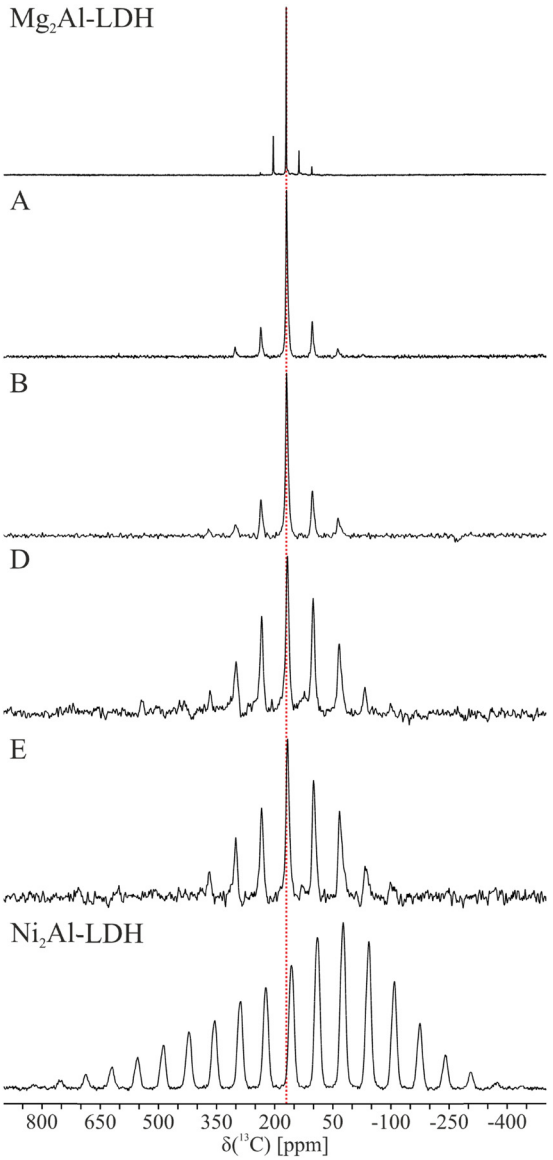

Fig. 5 ^{13}C MAS NMR spectra of the six the $Mg_{2-x}Ni_xAl$-LDH samples with x = 0 (Mg_2Al-LDH), 0.18 (A), 0.34 (B), 0.66 (D), 0.84 (E), and 2 (Ni_2Al-LDH) illustrating increased anisotropy with the Ni content. The red line indicates the isotropic chemical shift for the diamagnetic Mg_2Al-LDH. The NMR parameters obtained from the deconvolution of the spectra are reported in Table 2 and simulations using these parameters are shown in Fig. S4 (ESI†).

4. Experimental NMR results

The ^{13}C MAS NMR spectra of the six samples are shown in Fig. 5 and the principal components of the shielding tensor determined from analysis of the spinning sideband manifold are reported in Table 2. Given the 33% Al metal fraction in the current study, the carbonate (CO_3^{2-}) is expected to dominate as the interlayer anion, with only a small amount of bicarbonate (HCO_3^-).[15] This is unambiguously confirmed for diamagnetic Mg_2Al-LDH (Table 2). The bicarbonate has both an *approx.* 5 ppm lower shift and different sign of the Haeberlen chemical shift anisotropy, Δ, than carbonate in the interlayer of both

Table 2 The ^{13}C NMR chemical shift parameters (in ppm) for the $Mg_{2-x}Ni_xAl$-LDH samples with x = 0 (Mg_2Al-LDH), 0.18 (A), 0.34 (B), 0.68 (D), 0.84 (E), and 2 (Ni_2Al-LDH), as well as the two reference compounds sodium carbonate (Na_2CO_3) and sodium bicarbonate ($NaHCO_3$) using the standard convention, $\delta_{iso} = \frac{1}{3}(\delta_{11} + \delta_{22} + \delta_{33})$ with the principal values ordered as $\delta_{11} \geq \delta_{22} \geq \delta_{33}$. The spectra were recorded at room temperature or slightly above. Errors were estimated visually by varying the parameters and slightly changing the starting guess

Sample	x	δ_{11}	δ_{22}[a]	δ_{33}	δ
Na_2CO_3(s)	(Model)	205(4)	188(4)	119(4)	170.4(3)
$NaHCO_3$(s)	(Model)	227(2)	145(3)	121(3)	164.3(4)
Mg_2Al-LDH	0	200(4)	194(10)	117(3)	170.3(3)
A	0.18	264–267	161–148	94–81	170(2)
B	0.33	283–278	162–150	75–69	169(2)
D	0.68	342–339	159–145	3–1	167(4)
E	0.84	417–416	154–129	−45–−46	166(4)
Ni_2Al-LDH	2	637–636	51–48	−215–−216	156(4)

[a] It should be noted that δ_{22} is difficult to precisely determine experimentally, hence the indicated error margins are only indicative.

LDH and in sodium (bi)carbonate (Table S8, ESI†). This agrees with a recent study of ZnAl-LDH, which based on Rietveld refinement of PXRD data[19] obtained three possible monoclinic structures similar to 1M with one to three crystallographic inequivalent carbon sites, depending on the model and carbonate orientation. However, only a single ^{13}C resonance was observed experimentally for carbonate for the ZnAl-LDH investigated.

Visual inspection of ^{13}C MAS NMR spectra shows that only small changes are observed for the isotropic shift, as the difference between the Mg_2Al-LDH and Ni_2Al-LDH end members is 14 ppm. In contrast, the anisotropy seen, *e.g.*, in the number of spinning sidebands and the linewidth, to increase dramatically with the Ni^{2+} content. Simultaneously, a change is seen in the sign of the shielding anisotropy for sample A (x = 0.16). The elements of the chemical shift tensor were determined by fitting of the experimental spectra using a single site (See Fig. S4, ESI† and Table 2). This approach reproduced the spectra well at low Ni^{2+} contents, whereas some deviations are seen at high Ni contents especially for x = 0.84 and 2. This most likely reflects a distribution of the shielding parameters due to the presence of multiples sites in the different LDH polymorphs. Attempts to model the spectra with multiple sites proved ambiguous (six variables added per additional site). This effect is expected to be enhanced with the Ni content. For the low concentrations (x = 0.18 and 0.34), we observe a second site *ca.* 3 ppm lower, accounting for *ca.* 20–30% of the total intensity. However, this site is not observed for the diamagnetic Mg_2Al-LDH.

Assuming that the Ni^{2+} sites remain effectively magnetically uncoupled at the measurement temperature, as suggested by the ^{27}Al NMR shift data of the parent $Mg_{2-x}Ni_xAl$-LDH scaling linearly with the dopant concentration[14] (*vide supra*) one would expect a similar, linear dependence of also the experimental isotropic ^{13}C chemical shifts and shift eigenvalues of the interlayer carbonate anions on x. Taking into account the substantial size of the error margins in the data, this is roughly also observed.

While the conventional $R\bar{3}m$ crystal structure dictates axial symmetry of the ^{13}C shielding tensor, a significant asymmetry is observed, *cf.*, Table 2, which points to a lowering of the local symmetry in line with the detailed low-symmetry single-crystal X-ray structures (1M and 2T).[17,18] We note that the value of δ_{22} seems to be less precise especially for low Ni content (due to the spectra possessing few spinning side bands in this case) than

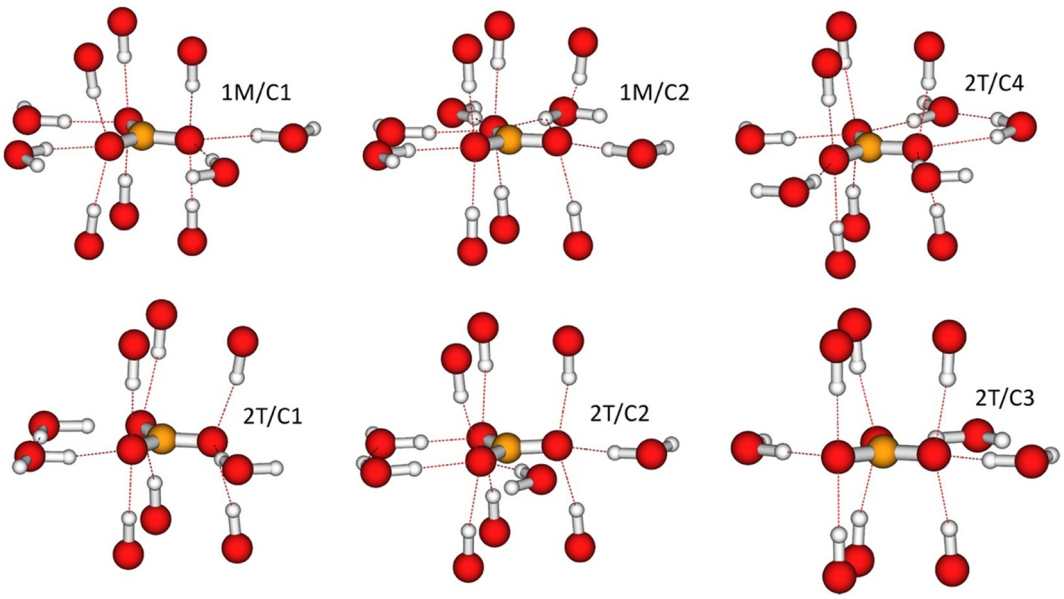

Fig. 6 The local hydrogen bonding network for the different CO_3^{2-} ions to the interlayer water molecules and hydroxyl groups in the cation layer in Mg_2Al-LDH using optimised structures. This is shown for the two crystallographic inequivalent carbon sites in the optimized 1M crystal structure (1M/C1 and 1M/C2) and the four carbon sites of the optimized 2T crystal structure. The 2T/C1 and 2T/C3 sites of the computations are two different instantaneous realisations (due to the different hydrogen-bonding pattern) of the same crystallographic position in the 2T structure.

the other two (δ_{11} and δ_{33}), which define the edges of the spectrum.

5. Computational results

Local environments and orbital shielding tensors

The local environments for all CO_3^{2-} resulting from the geometry-optimised 1M and 2T structures are illustrated in Fig. 6. $\boldsymbol{\sigma}_{orb}$ from the CASTEP calculations on the corresponding unit cells are given in Table S9 in the ESI.† A general feature of the optimised geometry is that the carbonate ions invariably seek themselves to the positions in which their oxygen ions are located directly between the M(II)$_2$Al–OH groups of the LDH layers both above and below. Thus, in addition to the in-plane hydrogen bonding with the water molecules, each oxygen "coordinates" both upwards and downwards to the OH groups of the adjacent LDH layers, with the distance of the carbonyl oxygen and the OH-group hydrogen in the range 1.78···1.87 Å. A second characteristic feature of the optimised geometry is that the carbonate ions remain parallel with the LDH layers.

Within the interlayer space, the oxygen atoms of the CO_3^{2-} ions are hydrogen-bonded to the hydrogen atoms of the water molecules in various patterns. In the 1M structure, two of the three oxygens for carbonates 1M/C1 and 1M/C2 are singly hydrogen-bonded to neighbouring water molecules, whereas the third oxygen of the 1M/C1 (1M/C2) carbonate is coordinated to two (three) waters. In the 2T structure, the carbonate sites 2T/C1 and 2T/C3 are singly hydrogen-bonded *via* two of their oxygen atoms, whereas the third oxygen is not hydrogen-bonded. The carbonate site 2T/C2 is singly hydrogen-bonded through two of its oxygens and twice bonded through a third oxygen. Hence, the bonding pattern is similar to that of the carbonate site C1 in the 1M structure. Finally, the carbonate site C4 of the 2T structure is doubly hydrogen-bonded to neighbouring waters *via* two of its oxygen atoms and singly hydrogen-bonded *via* the third atom. Hence, the altogether six carbon sites of the two structures represent four different hydrogen-bonding patterns, as detailed in Table 3.

In the $\boldsymbol{\sigma}_{orb}$ of all the carbon sites in both the 1M and 2T structures, the most shielded eigenvalue (σ_{33} = 47···48 ppm for 1M, 50···51 ppm for 2T) always points to the layer normal direction. The isotropic shielding constants are in all cases close to zero, due to the cancellation between the positive σ_{33} and negative (all σ_{11} and most σ_{22} eigenvalues, apart from the 1M/C2 site) eigenvalues. Three first hydrogen-bonding types in Table 3 form a systematic series where two of the oxygen atoms are always singly hydrogen bonded in the interlayer space, whereas the third oxygen atom evolves between non-bonded, double- and triple-bonded configurations. This development is reflected in $\boldsymbol{\sigma}_{orb}$: while the isotropic shielding constant becomes only slightly more positive, the shielding anisotropy $\Delta\sigma$ (with respect to the layer normal direction) goes through a clear decrease from 80 to 67 ppm and the asymmetry parameter, η, increases from 0.3 to 1 in the series. The fourth hydrogen-bonding situation breaks the pattern by featuring only one single-bonded and two double-bonded oxygens, and the resulting $\boldsymbol{\sigma}_{orb}$ again resembles the situation of the first case of Table 3. Hence, the hydrogen-bonding situation and the local environment of CO_3^{2-} are seen to be reflected primarily in the anisotropic properties of $\boldsymbol{\sigma}_{orb}$. The experimental spectra reflect an average of the different carbon sites with their hydrogen-bonding patterns, as the water molecules are dynamic on the NMR time scale at room temperature. Hence, the different sites in our model are best viewed as representing a selection of different instantaneous carbonate configurations and, thereby, the variation in NMR parameters.

Local hyperfine contributions

Table 4 lists the results for the isotropic ^{13}C hyperfine shielding constant $\boldsymbol{\sigma}_{con}$ from the local environment model depicted in Fig. 4. The corresponding data for the full shielding tensors is included in Table S10 (ESI†). In both Table 4 and Table S10 (ESI†), $\boldsymbol{\sigma}_{hf}$ denotes the result of the full quantum-chemical calculation using eqn (5), $\boldsymbol{\sigma}_{pc}^{(1)}$ is from PDA used for the Ni^{2+} centre, and $\boldsymbol{\sigma}_{con} = \boldsymbol{\sigma}_{hf} - \boldsymbol{\sigma}_{pc}^{(1)}$ is the double counting-eliminated total local hyperfine contribution to be added to the lattice summation results. The sites 1–8 are numbered according to an increasing distance from the ^{13}C site of the interlayer carbonate ion. Fig. 4(b) shows the spin density distribution of the closest site number 1, at the C–Ni distance of 3.7 Å. It is seen that the negative lobe of the spin density extends all the way from the

Table 3 The properties of the calculated orbital shielding tensor $\boldsymbol{\sigma}_{orb}$ (in ppm) for different carbon sites in the carbonate ions within computationally optimised 1M and 2T Mg_2Al-LDH structures. The hydrogen bonds between the carbonate ions and interlayer water molecules are summarised for each site

Carbonate sites	1M/C1	1M/C2	2T/C1[a]	2T/C3[a]	2T/C2	2T/C4
σ	−2.0	2.0	−2.6	−1.9	0.1	−2.0
σ_{11}[b]	48.3	46.5	50.8	51.4	50.2	49.9
σ_{22}[c]	−15.7	3.4	−21.3	−21.9	−8.5	−17.1
σ_{33}[c]	−38.5	−44.0	−37.5	−35.2	−41.3	−38.9
Hydrogen bonding	2 × single bonded, 1 × double bonded	2 × single bonded, 1 × triple bonded	2 × single bonded, 1 × no bond	2 × single bonded, 1 × no bond	2 × single bonded, 1 × double bonded	1 × single bonded, 2 × double bonded

[a] The 2T/C1 and 2T/C3 sites correspond to the same crystallographic site and are only distinguished in the computations due to the different instantaneous hydrogen-bonding situation with the interlayer water molecules in the computationally optimised structure. [b] The orbital shielding tensor eigenvalue corresponding to the direction along the LDH layer normal. [c] The orbital shielding tensor eigenvalues corresponding to the direction along the LDH layers. The eigenvalues are ordered such that $\sigma_{11} > \sigma_{22} > \sigma_{33}$.

Table 4 The calculated hyperfine contributions to the isotropic paramagnetic ^{13}C NMR shielding constant $\boldsymbol{\sigma}_{con}$ (in ppm) for the different Ni^{2+} positions in the cluster model depicted in Fig. 4(a). $\boldsymbol{\sigma}_{con}$ includes all the hyperfine contributions within the reach of the unpaired electron spin density distribution and which have not been fully included in the point-dipole model

			Hyperfine term[a]							
Ni^{2+} site number	r(Ni–C)/Å	Contribution	Contact (1 + 3)	Dipolar (2)	Orbital (4)	Contact + g-shift (6)	Dipolar + g-shift (7)	Contact + anis. g-shift (8)	Dipolar + anis. g-shift (9)	Total
1	3.70	σ_{hf}	17.12	−0.72	−0.05	1.76	−0.07	0.00	−1.01	17.03
		$\sigma_{pc}^{(1)}$	−1.11	−0.88	0.00	−0.11	−0.09	0.00	−1.23	−3.43
		σ_{con}	18.23	0.16	−0.05	1.87	0.02	0.00	0.23	20.45
2	4.04	σ_{hf}	9.31	−0.47	−0.03	0.96	−0.05	0.00	−0.66	9.06
		$\sigma_{pc}^{(1)}$	−0.70	−0.56	0.00	−0.07	−0.06	0.00	−0.78	−2.17
		σ_{con}	10.02	0.09	−0.03	1.03	0.01	0.00	0.12	11.23
3	4.13	σ_{hf}	7.13	−0.38	−0.03	0.73	−0.04	0.00	−0.54	6.87
		$\sigma_{pc}^{(1)}$	−0.58	−0.46	0.00	−0.06	−0.05	0.00	−0.64	−1.79
		σ_{con}	7.71	0.08	−0.03	0.79	0.01	0.00	0.10	8.66
4	4.67	σ_{hf}	3.25	−0.17	−0.01	0.33	−0.02	0.00	−0.24	3.13
		$\sigma_{pc}^{(1)}$	−0.25	−0.20	0.00	−0.03	−0.02	0.00	−0.27	−0.76
		σ_{con}	3.49	0.02	−0.01	0.36	0.00	0.00	0.03	3.89
5	4.81	σ_{hf}	3.98	−0.16	−0.01	0.41	−0.02	0.00	−0.22	3.98
		$\sigma_{pc}^{(1)}$	−0.22	−0.18	0.00	−0.02	−0.02	0.00	−0.25	−0.68
		σ_{con}	4.20	0.02	−0.01	0.43	0.00	0.00	0.02	4.66
6	4.92	σ_{hf}	3.21	−0.12	−0.01	0.33	−0.01	0.00	−0.17	3.23
		$\sigma_{pc}^{(1)}$	−0.17	−0.13	0.00	−0.02	−0.01	0.00	−0.19	−0.52
		σ_{con}	3.38	0.01	−0.01	0.35	0.00	0.00	0.02	3.75
7	5.10	σ_{hf}	0.65	−0.11	−0.01	0.07	−0.01	0.00	−0.16	0.43
		$\sigma_{pc}^{(1)}$	−0.14	−0.10	−0.01	0.41	−0.01	0.00	−0.14	0.01
		σ_{con}	0.79	−0.01	0.00	−0.34	0.00	0.00	−0.02	0.42
8	5.74	σ_{hf}	0.40	−0.03	0.00	0.04	0.00	0.00	−0.04	0.37
		$\sigma_{pc}^{(1)}$	−0.04	−0.03	0.00	0.00	0.00	0.00	−0.04	−0.12
		σ_{con}	0.44	0.00	0.00	0.05	0.00	0.00	0.01	0.49
Sum of 1···8		σ_{hf}	45.0	−2.2	−0.2	4.6	−0.2	0.0	−3.0	44.1
		$\sigma_{pc}^{(1)}$	−3.2	−2.5	0.0	0.1	−0.3	0.0	−3.5	−9.5
		σ_{con}	48.3	0.4	−0.1	4.5	0.0	0.0	0.5	53.6

[a] The numbering corresponds to the break-down of the hyperfine terms into physical contributions presented in ref. 39.

Ni^{2+} site to the ^{13}C centre, inducing a positive local contribution of $\boldsymbol{\sigma}_{hf}$ = 17.1 ppm to the isotropic shielding constant from this site, arising primarily from the contact hyperfine mechanism. When the shielding constant arising from PDA applied on this Ni^{2+} centre, $\boldsymbol{\sigma}_{pc}^{(1)}$ = −3.4 ppm, is subtracted from the result of the full quantum theory computation (eqn (5)), the local contribution that is not captured in the lattice summation process described below, amounts to $\boldsymbol{\sigma}_{con}$ = +20.5 ppm, for occupied site number one. The fact that the local contact density contribution is arising from negative spin density instead of the direct, positive contribution of the unpaired electrons, underlines the necessity of capturing the electron spin polarisation. Hence, an unrestricted computational method, such as the presently used unrestricted Kohn–Sham DFT procedure, is necessary.

The contributions of the sites 1–8 indicate a rapid reduction for the magnitude of the local hyperfine contributions with distance to the paramagnetic site. For example, the shielding constant is lowered to 0.5 ppm for site 8 located 5.74 Å from the carbon in the local model. For this site, after removal of the corresponding PDA contributions, the local contribution $\boldsymbol{\sigma}_{con}$ to be added to the lattice-summed $\boldsymbol{\sigma}_{pc}$ is +0.5 ppm, and we deduce that our model is sufficiently large to capture the essential local contributions. The sum of the sites 1–8 amounts to a total contribution of $\boldsymbol{\sigma}_{hf}$ = 44.1 ppm from the local model, converting to $\boldsymbol{\sigma}_{con}$ = +53.6 ppm when the PDA value is removed. Correspondingly, from the full tensors in Table S10 (ESI†) it is found that the total contribution of local paramagnetic sites 1···8 to the shielding anisotropy with respect to the LDH layer normal direction, $\Delta\sigma_{hf} = \sigma_{zz} - \frac{1}{2}(\sigma_{xx} - \sigma_{yy})$, equals no less than −1014 ppm. However, when the corresponding PDA value of $\Delta\sigma_{pc}^{(1)}$ = −1119 ppm is subtracted, $\Delta\boldsymbol{\sigma}_{con}$ = 105 ppm is left to be added as a local correction to the lattice summation of the PDA contributions. From all this, it is apparent that the spilling of negative spin density to the interlayer space and the consequent $\boldsymbol{\sigma}_{con}$ contributions to the ^{13}C shielding tensor of CO_3^{2-} are unexpectedly large and should be included in any

meaningful interpretation of the NMR of the intralayer species in such LDH materials. Moreover, this renders the interpretation of experimental T_1 relaxation data more complex, as the dipole approximation is violated.[56] One should note that the total numbers given above apply directly to 100% Ni^{2+} substitution to the M(II) sites of the cation layer and, in general the contributions scale linearly with the fractional Ni^{2+} concentration.

Total isotropic ^{13}C chemical shift

At this point we add the results of the lattice-summed δ_{pc} contributions, eqn (3). Fig. 7 compares the total calculated and experimental, isotropic ^{13}C chemical shifts for the different layer stacking models (1M and 2T) and different (X-ray based and geometry optimised) structures. Table 5 gives the associated numerical data. The results are given both excluding the local hyperfine correction, as $\delta_{orb} + \delta_{pc}$, and including the local hyperfine correction, as $\delta_{orb} + \delta_{pc} + \delta_{con}$. The computations assume that the paramagnetic Ni^{2+} ions are magnetically uncoupled. Therefore, a strictly linear dependence of the computed shift observables on x is expected and also obtained from the calculations. The computational isotropic δ_{iso} values start from *ca.* 10 ppm higher values than the experiment for the diamagnetic Mg_2Al-LDH parent compound. Errors of this magnitude may be expected from the DFT methodology used for the present calculations of $\boldsymbol{\sigma}_{orb}$. A comparison, however, of the calculations of an isolated CO_3^{2-} molecule with the presently employed PBE, a pure DFT functional, and the hybrid PBE0 functional (on the ORCA software) suggests that the use of PBE in the CASTEP calculation of $\boldsymbol{\sigma}_{orb}$ is not a major cause of the 10 ppm deviation from the experiment: the σ_{orb} obtained with the two functionals are within 1 ppm of each other. The shift computed as $\delta_{orb} + \delta_{pc}$ (the dotted lines in Fig. 7) increases linearly by 8 ppm in the compositional range x = 0–2, regardless of the underlying structure (1M or 2T), or whether the X-ray structure or computationally optimised geometries are used. Even after considering the estimated error margins, an increasing computational δ_{iso} is found, which contrasts the decreasing experimental trend as a function of x. As a result of the opposing trends, the deviation of the calculation from the experiment reaches up to *ca.* 30 ppm by reaching 100% substitution by Ni. As noted above, the experimental data is roughly linear as a function of x, at least considering the error margins, up to the concentration of x = 0.84. However, at 2 the experimental δ_{iso} falls below the linear trend.

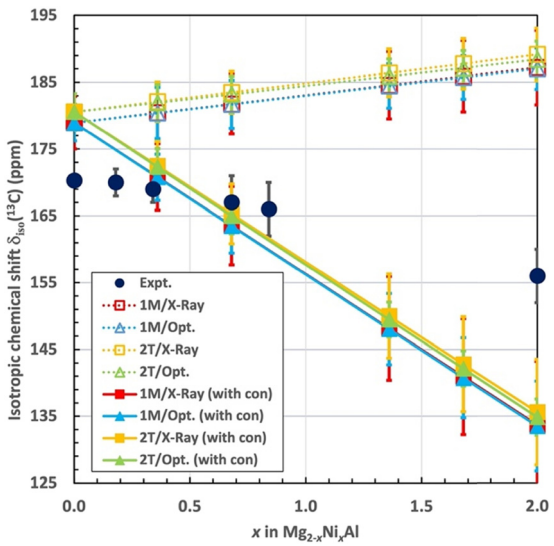

Fig. 7 Experimental and calculated isotropic chemical shift δ_{iso}(^{13}C) for CO_3^{2-} in $Mg_{2-x}Ni_xAl$-LDH as functions of x. The computational results are shown with (solid lines) and without (dotted lines) the local hyperfine contribution $\boldsymbol{\sigma}_{con}$.

Table 5 Calculated isotropic ^{13}C chemical shifts δ_{iso} (in ppm) for CO_3^{2-} in $Mg_{2-x}Ni_xAl$-LDH at different values of x. The values are averages of the C1 and C2 sites in the 1M structure, as well as the C1 to C4 in the 2T structure. The error margins of the computational data are assigned as the maximum differences of the site values for each case. Computational data include the orbital, pseudocontact and local hyperfine contributions

Method	Structure	x = 0	x = 0.36	x = 0.68	x = 1.36	x = 1.68	x = 2
$\delta_{orb} + \delta_{pc}$	1M/X-Ray	179(4)	180(4)	182(5)	185(5)	186(5)	187(6)
	1M/Opt.	179(4)	180(4)	182(4)	184(3)	186(3)	187(3)
	2T/X-ray	181(3)	182(3)	184(3)	186(4)	188(4)	189(4)
	2T/Opt.	181(3)	182(3)	183(3)	186(3)	187(3)	188(3)
$\delta_{orb} + \delta_{pc}$ + δ_{con}	1M/X-Ray	179(4)	171(5)	164(5)	148(6)	141(7)	134(8)
	1M/Opt.	179(4)	171(4)	163(4)	148(5)	141(5)	133(5)
	2T/X-Ray	181(3)	172(3)	165(4)	150(5)	143(5)	136(6)
	2T/Opt.	181(3)	172(3)	165(3)	149(4)	142(4)	135(5)

Incorporation of the $\boldsymbol{\sigma}_{con}$ contributions (the solid lines in Fig. 7) flips the trend of the computational results: now the isotropic δ_{iso} decreases with x, in qualitative agreement with the experiment. As also the δ_{con} term is simply proportional to x, the computed result at the diamagnetic limit remains roughly 10 ppm overestimated. While the error margins of the computational and experimental data overlap in the region of the intermediate x, at higher Ni^{2+} concentration, a significantly smaller shift is obtained than observed experimentally. The total computed change of the chemical shift from 0% to 100% Ni amounts to about −45 ppm, clearly overestimating the experimental value of −14.3 ppm. A possible reason for this error could be in the distance between the cation layers, 7.56 Å in the optimised 1M geometry, from which the local hyperfine model was calculated, to be compared with 7.63 and 7.56 Å in the experimental X-ray geometries of 1M and 2T, respectively. We tested the influence of the interlayer distance on the size of δ_{con} by calculations of the model with the closest paramagnetic site, number 1. In this test the interlayer distance was, in turn, extended and diminished by the difference of Δ = 0.06 Å between the experimental and optimised 1M geometries. The results are δ_{con}(site 1) = −21.6, −20.5 and −19.5 ppm for the models with diminished, "standard" and extended interlayer distance. This indicates that the δ_{con} contribution, which is dominated by the contact mechanism, decreases with increasing layer separation, as expected. The overall magnitude of the change amounts to 10% within the investigated distance range, implying that this structural parameter is important for the magnitude of the spin delocalisation to the interlayer species.

The obtained change is, nevertheless, too small to cause the overestimation of the decreasing trend of δ_{iso} with x in the present computations.

Total anisotropic ^{13}C chemical shift

The results for the anisotropic properties of the shielding tensors can be presented and compared to experiment in three distinct ways:

(1) Computed *eigenvalues* of the total $\boldsymbol{\delta}$ (including the $\boldsymbol{\delta}_{orb}$, $\boldsymbol{\delta}_{pc}$ and $\boldsymbol{\delta}_{con}$ contributions) are *averaged* over the 3000 generated Ni^{2+} distributions for, on the one hand, the two carbon sites of the 1M structure and, on the other hand, the four carbon sites of the 2T structure.

(2) Computed *eigenvalues* of the two carbon sites of the 1M structure and four carbon sites of the 2T structure are *averaged* over the Ni^{2+} distributions and presented *individually* site-by-site.

(3) Computed, full shielding *tensors* are *averaged* over the Ni^{2+} distributions between, on the one hand, the two sites of the 1M structure and, on the other hand, the four sites of the 2T structure, and the averaged tensors are then *subsequently diagonalised* to get the eigenvalues.

Methods 1 and 2 involve diagonalisation of the shielding tensor before averaging over sites and both 1M and 2T structures (in 1 and 2). In method 3, averaging of the tensors precedes diagonalisation. The distinction between the two distinct orders of averaging and diagonalisation has been discussed in ref. 57. Methods 1 and 2 are better suited for SSNMR studies on powder (polycrystalline) samples, where the principal values of the shift tensor are the primary observables. The difference between methods 1 and 2 is that the results are presented individually for all the ^{13}C sites in the latter. On the other hand, method 3 corresponds naturally to experiments on single-crystal samples. We choose to focus on method 1 in the following. The results of methods 2 and 3 are briefly discussed in the ESI.† In all cases, the shielding eigenvalues have been converted to chemical shifts.

Fig. 8 illustrates the averaged shift eigenvalues for the two sites of the 1M and for the four sites of the 2T structure. The numerical data are listed in Table 6. The computational shift eigenvalues are linear functions of x (positive slope for δ_{11}, negative for δ_{22} and δ_{33}). The experimental eigenvalues show a more complicated behaviour, albeit with similar trends when taking visually into account the error margins. The computational eigenvalues cross each other between zero Ni concentration and x = 0.36, which qualitatively matches the experimental observation (*vide supra*) of the different sign of the shielding anisotropy for sample A with x = 0.18, as compared to the samples with more Ni^{2+}. From that point onwards, the largest calculated shift eigenvalue, δ_{11}, always corresponds to the direction perpendicular to the LDH layers. The computations and experiments agree relatively well, taking into account the error margins of the computations (obtained as mentioned in Fig. 8).

As functions of x, the computations with only the $\boldsymbol{\delta}_{orb}$ and $\boldsymbol{\delta}_{pc}$ contributions (dashed lines and open symbols in Fig. 8) produce systematically too large slope of the shift eigenvalue for the direction perpendicular to the LDH layers (δ_{11}). Incorporation of the local hyperfine contribution $\boldsymbol{\delta}_{con}$ (full lines and symbols) significantly improves the overall agreement of the computed δ_{11} with the experimental data. For the full concentration (x = 2), the values of δ_{11} without and with the local

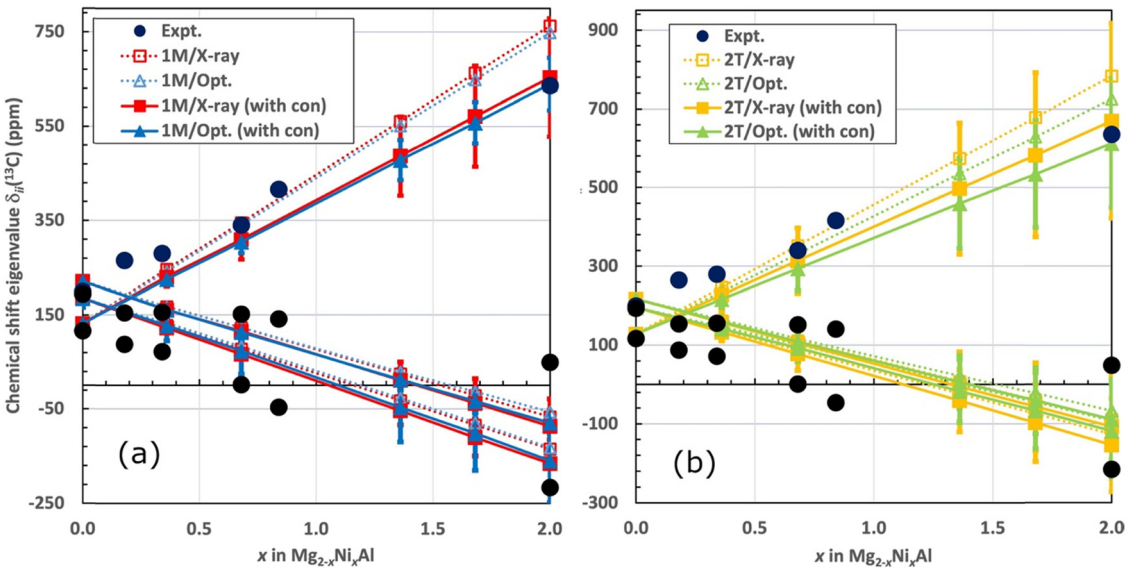

Fig. 8 The experimental and computed total ^{13}C chemical shift tensor eigenvalues (top to bottom: δ_{11}, δ_{22}, and δ_{33}, in ppm) for CO_3^{2-} in $Mg_{2-x}Ni_xAl$-LDH as functions of x. (a) 1M and (b) 2T structure. The computational results are shown both for the sum of orbital and pseudocontact contributions (dashed lines and open symbols) and added with local hyperfine contribution $\boldsymbol{\sigma}_{con}$ (full lines and symbols). Averaged eigenvalues are shown following method 1 described in the text. The error margins are placed on the full results (with $\boldsymbol{\sigma}_{con}$) based on the maximum difference between the corresponding eigenvalues from the different carbon sites (C1-2 for the 1M structure, C1-4 for 2T).

Table 6 Calculated ^{13}C NMR chemical shift eigenvalues (ppm) for $Mg_{2-x}Ni_xAl$-LDH as functions of x corresponding to Fig. 8, following method 1 described in the text. Data including orbital, pseudocontact and local hyperfine contributions

Structure	Eigenvalue	x = 0	x = 0.36	x = 0.68	x = 1.36	x = 1.68	x = 2
1M/X-ray	δ_{11}	132(2)	230(21)	310(43)	487(84)	571(107)	653(125)
	δ_{22}	220(6)	160(15)	115(24)	11(38)	−38(52)	−86(58)
	δ_{33}	185(19)	122(7)	66(5)	−53(31)	−111(39)	−166(51)
1M/Opt.	δ_{11}	132(2)	225(7)	304(23)	478(43)	558(43)	639(56)
	δ_{22}	220(6)	161(14)	113(15)	12(21)	−33(25)	−79(24)
	δ_{33}	185(19)	127(33)	73(50)	−46(74)	−102(78)	−159(89)
2T/X-ray	δ_{11}	128(1)	227(40)	314(83)	497(167)	583(208)	669(248)
	δ_{22}	218(4)	157(25)	104(46)	−6(88)	−56(112)	−108(130)
	δ_{33}	196(13)	133(22)	78(42)	−41(79)	−98(99)	−154(118)
2T/Opt.	δ_{11}	128(1)	216(26)	294(55)	459(115)	534(136)	613(164)
	δ_{22}	218(4)	160(12)	109(33)	6(67)	−41(85)	−89(102)
	δ_{33}	196(13)	141(19)	93(34)	−17(80)	−67(97)	−118(119)

hyperfine correction are 749 and 639 ppm, respectively, for the optimised geometry of the 1M structure. For the optimised 2T structure, the corresponding results are 726 and 613 ppm, to be compared with the experimental 636–637 ppm (Table 2). These numbers indicate that the effect of $\boldsymbol{\delta}_{con}$ is substantial. As in the case of isotropic δ_{iso} (*vide supra*), inclusion of the local hyperfine effect improves the agreement with experiment for the shift eigenvalue δ_{11} corresponding to the direction of the LDH layer normal. This effect results from the delocalisation of spin density into the carbon site of the interlayer anions and leads to semiquantitative agreement with experiment for this chemical shift eigenvalue.

The shift eigenvalues located in the plane of the LDH layers (δ_{22} and δ_{33}) become more negative as functions of increasing x. The effect of the local hyperfine contribution is, similarly to that on δ_{11}, to render the calculated δ_{22} and δ_{33} more negative than what is obtained with calculations involving the $\boldsymbol{\delta}_{orb}$ and $\boldsymbol{\delta}_{pc}$ contributions only (Fig. 8). The effect of $\boldsymbol{\delta}_{con}$ is, however, smaller for the in-plane eigenvalues than for δ_{11}: for the full Ni concentration the changes only amount to $-30\cdots-20$ ppm, depending on the structure. The agreement of the calculations with the full range of the experimental δ_{33} is very satisfactory. In contrast, for the middle eigenvalue, δ_{22}, all the calculated results, including the x = 2 end member of the series, are significantly more negative than the experimental numbers. This results also in the difference between the two computed in-plane eigenvalues to be systematically too small in comparison with experiment, *i.e.*, the shift asymmetry is underestimated by the present calculations. While the situation probably also reflects the fact that the middle eigenvalue is the most difficult to extract precisely from the experimental data, the underestimation of δ_{22} by the computations is paralleled by the exaggerated decreasing trend of the isotropic shift as a function of x, as discussed above. A possible cause of the lack of quantitative agreement with experiment in the present modelling, for the complete set of shielding observables, is the omission of molecular dynamics effects, primarily among the interlayer species.

Marginally improved agreement with experiment is obtained by using optimised structures as compared to the X-ray structures, as indicated by the triangle symbols (blue and green colour) in Fig. 8 being overall slightly closer to the experimental data points than the squares (red and yellow). The computational results for ^{13}C NMR shift eigenvalues in the 1M and 2T structural models are qualitatively similar. This matches the experimental observation one predominant ^{13}C resonance.

6. Conclusions

Detailed insight into the influence of paramagnetic Ni^{2+} ion on the ^{13}C NMR parameters was obtained for carbonate intercalated in a series of $Mg_{2-x}Ni_xAl$-LDH at various values of x from a combined experimental and computational study. Only small changes were observed for the isotropic chemical shifts (*ca.* 14 ppm for the Ni_2Al-LDH end member), which is readily determined experimentally and most often the only parameter reported. In contrast, a clear linear relationship with the Ni^{2+} content was observed for the tensor eigenvalues determined from detailed analysis of MAS NMR spectra. We devised a computational workflow in which quantum-chemical calculations were carried out including the orbital chemical shift combined with long-distance pseudocontact shifts obtained from a lattice sum averaged over randomly distributed paramagnetic sites, for which the magnetic susceptibility was computed *ab initio*, as well as the local hyperfine contribution to which the contact term makes a significant contribution.

A total of six different carbonate configurations stem from the models created for the 2T and 1M polymorphs, which provided detailed insight into how variations in the local hydrogen-bonding network affects the NMR shift parameters as a function of Ni^{2+} content. Experimentally, a single site dominated, which contains the average of these different positions. In the computations, only small variations (>2 ppm) were observed for the isotropic shifts arising from the orbital mechanism, whereas changes up to 10 ppm were obtained for the orbital shift eigenvalues. Larger effects up to hundreds of ppm in the eigenvalues were found from the paramagnetic hyperfine shift, where three computational methods differing

in the order of the matrix diagonalisation and averaging over the Ni dopant distribution and the individual carbon sites in these parent structures were applied in extracting the shift eigenvalue data. All the methods resulted by design in a linear dependence of the shielding eigenvalues on Ni^{2+} dopant concentration. It was mandatory to include local hyperfine effects resulting from delocalisation of the Ni^{2+} spin density, in addition to the expected orbital and pseudocontact contributions, to achieve good agreement with experiment for two of the three shift tensor eigenvalues. In contrast, the choice of using either experimental X-ray or computationally optimised crystal structures was found to be somewhat less crucial.

A qualitative agreement of theory with experiment was achieved in this, original computation of the NMR shielding tensor of the paramagnetic, Ni-doped solid solutions of LDH materials. While the results are not perfect, trends have been reproduced and valuable experience in the modelling of such complex inorganic materials has been gained. Near-quantitative agreement has been reached for two of the three ^{13}C shift eigenvalues as a result of incorporating the close-range hyperfine terms, primarily the contact contribution. This underlines the decisive role of the local hyperfine contribution. Consideration of molecular dynamics effects will be necessary in future modelling of NMR in the interlayer of LDH materials. The present work demonstrates that SSNMR combined with computational modelling with the presently introduced methodology can provide detailed insight into paramagnetic LDH and other complex layered materials.

Author contributions

MM and JM did the programming of the lattice summation model. MM performed all the quantum-chemical calculations, curated the computational data and contributed to the writing of the manuscript. JM assisted in the pNMR analysis and graphics. JV and UGN conceptualised the project, contributed to writing the manuscript and supervised the work. ABAA in collaboration with UGN and NDJ performed analysis of the experimental ^{13}C SSNMR spectra. NDJ and UGN synthesized the ^{13}C labelled LDH and recorded the ^{13}C NMR data. The manuscript was commented and refined by all the authors.

Conflicts of interest

There are no conflicts to declare.

Acknowledgements

Dr Tae-Hyun Kim is acknowledged for the preparation of the Mg_2Al-LDH precursor and Prof. Christine Taviot-Gueho for useful discussion regarding LDH polymorphism. Dr Elena Zhitova (Russian Academy of Science) is acknowledged for kindly sharing crystallographic data and useful information. We acknowledge funding from the Academy of Finland (grant 331008) and University of Oulu (Kvantum Institute, MM, JM, JV), European Union's Horizon 2020 research and innovation programme under the Marie Skłodowska–Curie (grant agreement no. 713606, MM), the Danish Council for Independent Research Science and Universe (grant DFF-7014-00198; UGN, ABAA, JV). Computations were carried at CSC-the Finnish IT Centre for Science and the Finnish Grid and Cloud Infrastructure project (persistent identifier urn:nbn:fi:research-infras-2016072533).

References

1 C. Depège, F. Z. El Metoui, C. Forano, A. De Roy, J. Dupuis and J. P. Besse, Polymerization of silicates in layered double hydroxides, *Chem. Mater.*, 1996, **8**, 952–960.
2 D. G. Evans and R. C. T. Slade, Structural aspects of layered double hydroxides, *Struct. Bond.*, 2005, **119**, 1–87.
3 J. Zhong, B. Hou, W. Zhang, Z. Guo and C. Zhao, Investigation on the physical and electrochemical properties of typical Ni-based alloys used for the bipolar plates of proton exchange membrane fuel cells, *Heliyon*, 2023, **9**, e16276.
4 S. Britto and P. V. Kamath, Polytypism, disorder, and anion exchange properties of divalent ion (Zn, Co) containing bayerite-derived layered double hydroxides, *Inorg. Chem.*, 2010, **49**, 11370–11377.
5 K. H. Goh, T. T. Lim and Z. Dong, Application of layered double hydroxides for removal of oxyanions: A review, *Water Res.*, 2008, **42**, 1343–1368.
6 G. R. Williams, T. G. Dunbar, A. J. Beer, A. M. Fogg and D. O'Hare, Intercalation chemistry of the novel layered double hydroxides $[MAl_4(OH)_{12}](NO_3)_2{\cdot}yH_2O$ (M = Zn, Cu, Ni and Co). 2: Selective intercalation chemistry, *J. Mater. Chem.*, 2006, **16**, 1231–1237.
7 G. R. Williams, T. G. Dunbar, A. J. Beer, A. M. Fogg and D. O'Hare, Intercalation chemistry of the novel layered double hydroxides $[MAl_4(OH)_{12}](NO_3)_2{\cdot}yH_2O$ (M = Zn, Cu, Ni and Co). 1: New organic intercalates and reaction mechanisms, *J. Mater. Chem.*, 2006, **16**, 1222–1230.
8 S. Bégu, A. Aubert-Pouëssel, R. Polexe, E. Leitmanova, D. A. Lerner, J. M. Devoisselle and D. Tichit, New layered double hydroxides/phospholipid bilayer hybrid material with strong potential for sustained drug delivery system, *Chem. Mater.*, 2009, **21**, 2679–2687.
9 F. Cavani, F. Trifirò and A. Vaccari, Hydrotalcite-type anionic clays: Preparation, properties and applications, *Catal. Today*, 1991, **11**, 173–301.
10 C. Taviot-Guého, P. Vialat, F. Leroux, F. Razzaghi, H. Perrot, O. Sel, N. D. Jensen, U. G. Nielsen, S. Peulon, E. Elkaim and C. Mousty, Dynamic Characterization of Inter- and Intralamellar Domains of Cobalt-Based Layered Double Hydroxides upon Electrochemical Oxidation, *Chem. Mater.*, 2016, **28**, 7793–7806.
11 S. Radha and P. V. Kamath, Structural synthon approach to predict the possible polytypes of layered double hydroxides, *Z. Anorg. Allg. Chem.*, 2012, **638**, 2317–2323.

12 U. G. Nielsen, Chapter Two-Solid state NMR studies of layered double hydroxides, *Annu. Rep. NMR Spectrosc.*, 2021, **104**, 75–140.
13 P. J. Sideris, U. G. Nielsen, Z. Gan and C. P. Grey, Mg/Al ordering in layered double hydroxides revealed by multinuclear NMR spectroscopy, *Science*, 2008, **321**, 113–117.
14 N. D. Jensen, C. Forano, S. S. C. Pushparaj, Y. Nishiyama, B. Bekele and U. G. Nielsen, The distribution of reactive Ni^{2+} in 2D $Mg_{2-x}Ni_xAl$-LDH nanohybrid materials determined by solid state ^{27}Al MAS NMR spectroscopy, *Phys. Chem. Chem. Phys.*, 2018, **20**, 25335–25342.
15 A. Di Bitetto, G. Kervern, E. André, P. Durand and C. Carteret, Carbonate–Hydrogenocarbonate Coexistence and Dynamics in Layered Double Hydroxides, *J. Phys. Chem. C*, 2017, **121**, 6104–6112.
16 S. Ishihara, P. Sahoo, K. Deguchi, S. Ohki, M. Tansho, T. Shimizu, J. Labuta, J. P. Hill, K. Ariga, K. Watanabe, Y. Yamauchi, S. Suehara and N. Iyi, Dynamic breathing of CO_2 by hydrotalcite, *J. Am. Chem. Soc.*, 2013, **135**, 18040–18043.
17 S. V. Krivovichev, V. N. Yakovenchuk, E. S. Zhitova, A. A. Zolotarev, Y. A. Pakhomovsky and G. Y. Ivanyuk, Crystal chemistry of natural layered double hydroxides. I. Quintinite-2H-3c from the Kovdor alkaline massif, Kola peninsula, Russia, *Mineral. Mag.*, 2010, **74**, 821–832.
18 E. S. Zhitova, S. V. Krivovichev, V. N. Yakovenchuk, G. Y. Ivanyuk, Y. A. Pakhomovsky and J. A. Mikhailova, Crystal chemistry of natural layered double hydroxides: 4. Crystal structures and evolution of structural complexity of quintinite polytypes from the Kovdor alkaline-ultrabasic massif, Kola peninsula, Russia, *Mineral. Mag.*, 2018, **82**, 329–346.
19 S. Radhakrishnan, K. Lauwers, C. V. Chandran, J. Trébosc, S. Pulinthanathu Sree, J. A. Martens, F. Taulelle, C. E. A. Kirschhock and E. Breynaert, NMR Crystallography Reveals Carbonate Induced Al-Ordering in ZnAl Layered Double Hydroxide, *Chem. – Eur. J.*, 2021, **27**, 15944–15953.
20 A. Lund, G. V. Manohara, A. Y. Song, K. M. Jablonka, C. P. Ireland, L. A. Cheah, B. Smit, S. Garcia and J. A. Reimer, Characterization of Chemisorbed Species and Active Adsorption Sites in Mg-Al Mixed Metal Oxides for High-Temperature CO_2 Capture, *Chem. Mater.*, 2022, **34**, 3893–3901.
21 A. B. A. Andersen, C. Henriksen, Q. Wang, D. B. Ravnsbæk, L. P. Hansen and U. G. Nielsen, Synthesis and Thermal Degradation of $MAl_4(OH)_{12}SO_4{\cdot}3H_2O$ with M = Co^{2+}, Ni^{2+}, Cu^{2+}, and Zn^{2+}, *Inorg. Chem.*, 2021, **60**, 16700–16712.
22 S. Ishihara, K. Deguchi, H. Sato, M. Takegawa, E. Nii, S. Ohki, K. Hashi, M. Tansho, T. Shimizu, K. Ariga, J. Labuta, P. Sahoo, Y. Yamauchi, J. P. Hill, N. Iyi and R. Sasai, Multinuclear solid-state NMR spectroscopy of a paramagnetic layered double hydroxide, *RSC Adv.*, 2013, **3**, 19857–19860.
23 T.-H. Kim, L. Lundehøj and U. G. Nielsen, An investigation of the phosphate removal mechanism by MgFe layered double hydroxides, *Appl. Clay Sci.*, 2020, **189**, 105521.
24 T. Charpentier, The PAW/GIPAW approach for computing NMR parameters: A new dimension added to NMR study of solids, *Solid State Nucl. Magn. Reson.*, 2011, **40**, 1–20.
25 J. Xu, X. Liu, X. Liu, T. Yan, H. Wan, Z. Cao and J. A. Reimer, Deconvolution of metal apportionment in bulk metal-organic frameworks, *Sci. Adv.*, 2022, **8**, 1–9.
26 I. Bertini, C. Luchinat, G. Parigi and E. Ravera, Solution NMR of Paramagnetic Molecules: Applications to Metallobiomolecules and Models, Elsevier Sci, 2016.
27 Kamilla Thingholm Bünning, University of Southern Denmark, 2021.
28 S. G. J. van Meerten, W. M. J. Franssen and A. P. M. Kentgens, ssNake: A cross-platform open-source NMR data processing and fitting application, *J. Magn. Reson.*, 2019, **301**, 56–66.
29 R. Boča, *Theoretical foundations of molecular magnetism*, Elsevier, 1999.
30 K. Momma and F. Izumi, VESTA 3 for three-dimensional visualization of crystal, volumetric and morphology data, *J. Appl. Crystallogr.*, 2011, **44**, 1272–1276.
31 S. V. Krivovichev, V. N. Yakovenchuk, E. S. Zhitova, A. A. Zolotarev, Y. A. Pakhomovsky and G. Y. Ivanyuk, Crystal chemistry of natural layered double hydroxides. 2. Quintinite-1M: first evidence of a monoclinic polytype in M^{2+}-M^{3+} layered double hydroxides, *Mineral. Mag.*, 2010, **74**, 833–840.
32 S. J. Clark, M. D. Segall, C. J. Pickard, P. J. Hasnip, M. I. J. Probert, K. Refson and M. C. Payne, First principles methods using CASTEP, *Zeitschrift fur Krist.*, 2005, **220**, 567–570.
33 J. P. Perdew, K. Burke and M. Ernzerhof, Generalized gradient approximation made simple, *Phys. Rev. Lett.*, 1996, **77**, 3865–3868.
34 S. Grimme, Semiempirical GGA-type density functional constructed with a long-range dispersion correction, *J. Comput. Chem.*, 2006, **27**, 1787–1799.
35 D. D. Koelling and B. N. Harmon, A technique for relativistic spin-polarised calculations, *J. Phys. C-Solid State Phys.*, 1977, **10**, 3107.
36 H. J. Monkhorst and J. D. Pack, Special points for Brillouin-zone integrations, *Phys. Rev. B: Solid State*, 1976, **13**, 5188–5192.
37 C. J. Pickard and F. Mauri, All-electron magnetic response with pseudopotentials: NMR chemical shifts, *Phys. Rev. B: Condens. Matter Mater. Phys.*, 2001, **63**, 2451011–2451013.
38 J. R. Yates, C. J. Pickard and F. Mauri, Calculation of NMR chemical shifts for extended systems using ultrasoft pseudopotentials, *Phys. Rev. B: Condens. Matter Mater. Phys.*, 2007, **76**, 24401.
39 J. Vaara, S. A. Rouf and J. Mareš, Magnetic Couplings in the Chemical Shift of Paramagnetic NMR, *J. Chem. Theory Comput.*, 2015, **11**, 4840–4849.
40 R. J. Kurland and B. R. McGarvey, Isotropic NMR shifts in transition metal complexes: The calculation of the Fermi contact and pseudocontact terms, *J. Magn. Reson.*, 1970, **2**, 286–301.
41 A. Soncini and W. Van den Heuvel, Communication: Paramagnetic NMR chemical shift in a spin state subject to zero-field splitting, *J. Chem. Phys.*, 2013, **138**, 21103.

42 B. Martin and J. Autschbach, Temperature dependence of contact and dipolar NMR chemical shifts in paramagnetic molecules, *J. Chem. Phys.*, 2015, **142**, 54108.
43 L. Lang, E. Ravera, G. Parigi, C. Luchinat and F. Neese, Solution of a Puzzle: High-Level Quantum-Chemical Treatment of Pseudocontact Chemical Shifts Confirms Classic Semiempirical Theory, *J. Phys. Chem. Lett.*, 2020, **11**, 8735–8744.
44 L. Benda, J. Mareš, E. Ravera, G. Parigi, C. Luchinat, M. Kaupp and J. Vaara, Pseudo-Contact NMR Shifts over the Paramagnetic Metalloprotein CoMMP-12 from First Principles, *Angew. Chemie*, 2016, **128**, 14933–14937.
45 J. Sauer, Molecular Models in ab Initio Studies of Solids and Surfaces: From Ionic Crystals and Semiconductors to Catalysts, *Chem. Rev.*, 1989, **89**, 199–255.
46 A. B. A. Andersen, R. T. Christiansen, S. Holm-Janas, A. S. Manvell, K. S. Pedersen, D. Sheptyakov, J. P. Embs, H. Jacobsen, E. Dachs, J. Vaara, K. Lefmann and U. G. Nielsen, The magnetic properties of $MAl_4(OH)_{12}SO_4{\cdot}3H_2O$ with M = Co^{2+}, Ni^{2+}, and Cu^{2+} determined by a combined experimental and computational approach, *Phys. Chem. Chem. Phys.*, 2023, **25**, 3309–3322.
47 F. Neese, The ORCA program system, *Wiley Interdiscip. Rev.: Comput. Mol. Sci.*, 2012, **2**, 73–78.
48 M. Douglas and N. M. Kroll, Quantum electrodynamical corrections to the fine structure of helium, *Ann. Phys. (N. Y).*, 1974, **82**, 89–155.
49 B. A. Hess, Relativistic electronic-structure calculations employing a two-component no-pair formalism with external-field projection operators, *Phys. Rev. A*, 1986, **33**, 3742–3748.
50 D. Ganyushin and F. Neese, A fully variational spin-orbit coupled complete active space self-consistent field approach: Application to electron paramagnetic resonance *g*-tensors, *J. Chem. Phys.*, 2013, **138**, 104113.
51 D. Ganyushin and F. Neese, First-principles calculations of zero-field splitting parameters, *J. Chem. Phys.*, 2006, **125**, 24103.
52 C. Angeli, R. Cimiraglia and J. P. Malrieu, N-electron valence state perturbation theory: A fast implementation of the strongly contracted variant, *Chem. Phys. Lett.*, 2001, **350**, 297–305.
53 C. Angeli, R. Cimiraglia, S. Evangelisti, T. Leininger and J.-P. Malrieu, Introduction of n-electron valence states for multireference perturbation theory, *J. Chem. Phys.*, 2001, **114**, 10252–10264.
54 C. Angeli, R. Cimiraglia and J.-P. Malrieu, n-electron valence state perturbation theory: A spinless formulation and an efficient implementation of the strongly contracted and of the partially contracted variants, *J. Chem. Phys.*, 2002, **117**, 9138–9153.
55 F. Weigend and R. Ahlrichs, Balanced basis sets of split valence, triple zeta valence and quadruple zeta valence quality for H to Rn: Design and assessment of accuracy, *Phys. Chem. Chem. Phys.*, 2005, **7**, 3297–3305.
56 A. B. A. Andersen, A. Pyykkönen, H. J. Aa. Jensen, V. McKee, J. Vaara and U. G. Nielsen, Remarkable reversal of ^{13}C-NMR assignment in d^1, d^2 compared to d^8, d^9 acetylacetonate complexes: Analysis and explanation based on solid-state MAS NMR and computations, *Phys. Chem. Chem. Phys.*, 2020, **22**, 8048–8059.
57 T. S. Pennanen, J. Vaara, P. Lantto, A. J. Sillanpää, K. Laasonen and J. Jokisaari, Nuclear Magnetic Shielding and Quadrupole Coupling Tensors in Liquid Water: A Combined Molecular Dynamics Simulation and Quantum Chemical Study, *J. Am. Chem. Soc.*, 2004, **126**, 11093–11102.

